



Article

# Assessment of the Impact of Reservoirs in the Upper Mekong River Using Satellite Radar Altimetry and Remote Sensing Imageries

Kuan-Ting Liu<sup>1</sup>, Kuo-Hsin Tseng<sup>1,2,3,\*</sup>, C. K. Shum<sup>4,5</sup>, Chian-Yi Liu<sup>2,6</sup>, Chung-Yen Kuo<sup>7</sup>, Ganming Liu<sup>5</sup>, Yuanyuan Jia<sup>5</sup> and Kun Shang<sup>5</sup>

<sup>1</sup> Department of Civil Engineering, National Central University, 32001 Taoyuan, Taiwan; 103322086@cc.ncu.edu.tw

<sup>2</sup> Center for Space and Remote Sensing Research, National Central University, 32001 Taoyuan, Taiwan; cyliu@csrsr.ncu.edu.tw

<sup>3</sup> Institute of Hydrological and Oceanic Sciences, National Central University, 32001 Taoyuan, Taiwan

<sup>4</sup> State Key Laboratory of Geodesy and Earth's Dynamics, Institute of Geodesy and Geophysics, Chinese Academy of Sciences, 430077 Wuhan, China; ckshum@osu.edu

<sup>5</sup> Division of Geodetic Science, School of Earth Sciences, Ohio State University, Columbus, OH 43210, USA; liu.669@osu.edu (G.L.); jia.102@osu.edu (Y.J.); shang.34@osu.edu (K.S.)

<sup>6</sup> Department of Atmospheric Sciences, National Central University, 32001 Taoyuan, Taiwan

<sup>7</sup> Department of Geomatics, National Cheng Kung University, 70101 Tainan, Taiwan; Kuo70@mail.ncku.edu.tw

\* Correspondence: khtseng@csrsr.ncu.edu.tw; Tel.: +886-3422-7151

Academic Editors: Cheinway Hwang, Wenbin Shen, Stéphane Calmant, Magaly Koch and Prasad S. Thenkabail  
Received: 29 February 2016; Accepted: 20 April 2016; Published: 28 April 2016

**Abstract:** Water level (WL) and water volume (WV) of surface-water bodies are among the most crucial variables used in water-resources assessment and management. They fluctuate as a result of climatic forcing, and they are considered as indicators of climatic impacts on water resources. Quantifying riverine WL and WV, however, usually requires the availability of timely and continuous *in situ* data, which could be a challenge for rivers in remote regions, including the Mekong River basin. As one of the most developed rivers in the world, with more than 20 dams built or under construction, Mekong River is in need of a monitoring system that could facilitate basin-scale management of water resources facing future climate change. This study used spaceborne sensors to investigate two dams in the upper Mekong River, Xiaowan and Jinghong Dams within China, to examine river flow dynamics after these dams became operational. We integrated multi-mission satellite radar altimetry (RA, Envisat and Jason-2) and Landsat-5/-7/-8 Thematic Mapper (TM)/Enhanced Thematic Mapper plus (ETM+)/Operational Land Imager (OLI) optical remote sensing (RS) imageries to construct composite WL time series with enhanced spatial resolutions and substantially extended WL data records. An empirical relationship between WL variation and water extent was first established for each dam, and then the combined long-term WL time series from Landsat images are reconstructed for the dams. The  $R^2$  between altimetry WL and Landsat water area measurements is  $>0.95$ . Next, the Tropical Rainfall Measuring Mission (TRMM) data were used to diagnose and determine water variation caused by the precipitation anomaly within the basin. Finally, the impact of hydrologic dynamics caused by the impoundment of the dams is assessed. The discrepancy between satellite-derived WL and available *in situ* gauge data, in term of root-mean-square error (RMSE) is at 2–5 m level. The estimated WV variations derived from combined RA/RS imageries and digital elevation model (DEM) are consistent with results from *in situ* data with a difference at about 3%. We concluded that the river level downstream is affected by a combined operation of these two dams after 2009, which has decreased WL by  $0.20 \text{ m} \cdot \text{year}^{-1}$  in wet seasons and increased WL by  $0.35 \text{ m} \cdot \text{year}^{-1}$  in dry seasons.

**Keywords:** Mekong River; water level; satellite radar altimetry; optical satellite images

## 1. Introduction

Mekong River (MR), also called Lancang River in China, originates from the eastern Qinghai-Tibetan Plateau (TP) (Figure 1) and is ranked as the 10th longest river in the world. The region where headwater forms is also called the Three Rivers Nature Reserve, where the stream later diverts into two other major rivers in China: the Yangtze and Yellow Rivers. This reserve area is formed by steep terrain with an average altitude at 4000 m and abundant alpine glaciers. The MR is a transboundary river running through six countries in Southeast Asia, including China, Myanmar, Laos, Thailand, Cambodia, and Vietnam, with a broad watershed covering  $8 \times 10^5 \text{ km}^2$  and an average annual total discharge of  $\sim 4.5 \times 10^{11} \text{ m}^3$ . The MR is also the sixth largest in the world regarding annual flow [1]. In Southeast Asia, especially in the upper MR, water resources are limited; hence, most of the countries demarcated by the river intend to impound water within their territories.



**Figure 1.** Locations of the Mekong River (navy blue) and its watershed (yellow shaded area). The river was originated from the southeast of the Qinghai-Tibetan Plateau (boundary depicted by red borders). The background used TrueMarble imagery, with terrain elevation enhancement by NOAA ETOPO1 global digital elevation model (DEM). This figure was plotted using the Generic Mapping Tool (GMT) version 5, which is available from [2]. GMT is an open source tool collection for manipulating geographic and Cartesian data sets [3].

The headwater of MR reaches an elevation of 5,000 m and drops to about 355 m when it passes through Thailand. The topography is thus suitable for hydropower development. The MR has a hydropower potential of about 53,000 MW [4]. Hence, several dams were built on multiple tributaries in the basin for domestic usage, irrigation, and hydropower generation (Figure 2, red squares). Over the last few years, frequent local news posts were noticed regarding the operation of these dams that keep water draining from the TP to generate electricity. There are only a few studies focused on the

impacts caused by a cascade of dams on the upper Mekong River [5,6]. For example, Räsänen *et al.* [5] in 2012 used a hydrological model and an optimization scheme to assess the impacts and found that the construction of dams changes the flow regime of the MR. Their analysis showed that the discharge increased by 34%–155% in dry seasons and decreased by 29%–36% in wet seasons at Chiang Saen, Thailand. Another study, conducted by the International Rivers organization [6,7], analyzed the impact on broader aspects, such as fisheries, agriculture, and erosion. They mentioned that the construction of Xiaowan Dam would block 35% of silt, which should have nourished the downstream floodplains. Without using artificial fertilizer, the long-term agricultural yields would decrease.

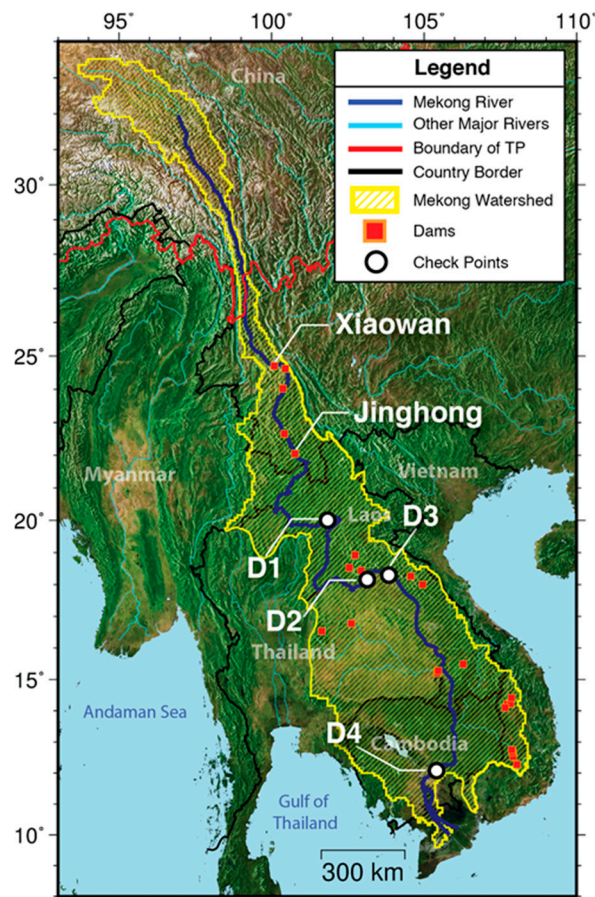


**Figure 2.** Location map of the Mekong River and study area. Combined altimetry and Landsat imageries to derive WL are performed at Xiaowan and Jinghong Dams. Four checkpoints (D1–D4) are used to inspect the change of river flow after dam constructions. D1–D3 have both Envisat and Jason-2 crossovers nearby, while D4 has only Jason-2.

Water level (WL) and water volume (WV) are among the most crucial physical quantities for water resources management, and also are indicators of the impact of climate change. The traditional and straightforward approach to monitor WL is to use locally *in situ* gauge or stage stations. They would provide continuous and reliable WL measurements at locations along the river. However, primarily due to the length and remoteness of the MR, it would be difficult to install and maintain adequate gauge stations to monitor the entire river. More importantly, other issues associated with economic/political restrictions/data latency would also result in data inaccessibility in different countries. The feasibility to obtain timely and continuous observations at multiple sections along the river remains a challenge. These issues are highlighted, for example, in reports published by the Mekong River Commission (MRC, [8]). The MRC is an inter-governmental organization that works with governments of Cambodia, Laos, Thailand and Vietnam, and creates a joint management of water

resources and sustainable development. The data released by the MRC include gauge WL, discharge measurements, water quality, and drought information mainly in the lower Mekong watershed. However, because China is not a member of MRC, there is only one gauge located at Jinghong on the upper MR providing WL measurements of the dam. Moreover, the data only covered a limited period after the impoundment, which hinders the knowledge of downstream water availability. Another source of local data is released from HydroLancang, a subsidiary of the China Huaneng Group that manages the construction and maintenance of hydropower along the Lancang River in the upper MR. At some phases of dam construction, HydroLancang updates the WL records.

In order to monitor such an important yet poorly understood watershed, this study proposes to use timely satellite measurements at low-cost with reliable data quality. Recent advances in geodetic satellite technology allow spaceborne sensors to be a feasible means to retrieve inland WL for adequately wide rivers. Satellite radar altimetry (RA) is a technology originally developed for ocean surface topography observations and large-scale circulation studies [9–11]. This technology was also applied to sea-ice freeboard, ice-sheet, glacier, and even crustal elevation observations [12–18]. Since the first altimeter onboard NASA's Skylab launched in 1973, there have been, and presently continue to be, abundant concurrent and successive RA satellites operated or operating in space. While satellite hydrology is viable using satellite RA for large inland waterbodies, radar waveforms over smaller inland waterbodies are contaminated by land features resulting in degraded accuracy or altimeter losing lock. Several waveform retracking algorithms have been developed to overcome the signal contamination problem. Using customized algorithms (physical or empirical methods) to locate the midpoint of the leading edge in a waveform, corresponding to the time elapse of radar pulse reached mean Earth's surface within radar footprint. Satellite RA can thus be applied to inland water observation using these waveform retracking methods and also other data processing advances [19–23]. The accuracy of RA over narrow rivers/small lakes (<1 km) generally ranges between 0.32 and 0.72 m [24,25].

However, satellite RA is still limited by its long revisit periods, e.g., monthly sampling, or if the repeat period were reduced to 10 days, the cross-track spatial resolution would be coarser. Altimetry satellite by design is to have exact repeat tracks over the ocean to remove geoid errors and monitor sea level variations periodically, but the frozen orbit also leads to long revisit period or large cross-track distances between neighboring ground tracks. These limitations cause temporal or spatial gaps during each altimeter overpass. The plausible spatial-temporal resolution improvement for remotely sensed WL observations from satellite altimetry thus becomes a challenging objective. Here, the study proposed an indirect method to utilize multiple sensors with different respective strength and accuracy. We integrated RA satellites, RS imageries and a digital elevation model (DEM) to generate empirical relationships between WL, water area (WA) and WV changes. With this relationship, the combined data sets can be used to monitor WL and WV variations over the study region with long-term time series and improved spatial resolutions. Once satellite imageries could be converted to WL measurements, it potentially densifies the temporal data points and provides much longer time series (~40 years), as compared with altimeter data span (~26 years).

The overall purpose of this study is to investigate the impact of dams on downstream water resources in the MR from satellite observations. We demonstrate the combined RA/RS observed hydrologic quantities in two locations, the Xiaowan and Jinghong Dams in the upper MR, to monitor WL changes during impoundment and the regular operations afterward. We also checked the river flow at four locations downstream to assess the impact due to Dam operations. The study area is briefly described in Section 2. Satellite altimetry, Landsat optical RS, and rainfall data used herein and processing method are described in Section 3. The major findings on the dam affected downstream WL are discussed in Section 4. Finally, the discussion of dam-impacted downstream hydrologic schemes in the MR and conclusions are given in Sections 5 and 6 respectively.

## 2. Study Area

There are over 20 dams built or under construction by adjacent countries at different sections of the MR [26]. China controls the upmost part of the river, and its dam construction is the largest compared to downstream countries. This study focuses on two major hydropower stations in the upper MR, Xiaowan (100.09°E, 24.70°N) and Jinghong Dam (100.77°E, 22.05°N). Our purpose is to compare the WL time series at these two locations and sites in the downstream area, to evaluate the impact of dams during their constructions, commissioning and fully operating phases. In fact, there are at least three more dams located between Xiaowan and Jinghong, which are Manwan (operated since 1995), Dachaoshan (2003), and Nuozhadu (2013) dams. However, because satellite data are limited for Manwan Dam constructed in earlier years, while Dachaoshan is relatively small with a total capacity of about  $1 \times 10^8 \text{ m}^3$ , and Nuozhadu Dam was only operational after 2013, they have been excluded from this analysis. Nevertheless, we believe a focus of the most upstream (Xiaowan) and downstream (Jinghong) dams along the upstream of MR is sufficient to generalize the impact of other dams further downstream.

The Xiaowan Dam is an arch dam whose purpose is mainly to generate hydropower. It supports a 4200 MW power station. The construction began in 2002 and finished in 2010. It is the second highest dam (292 m) in the world with a nominal total capacity of  $153 \times 10^8 \text{ m}^3$ . The Jinghong Dam has a 1750 MW power station and a smaller total capacity of  $14 \times 10^8 \text{ m}^3$ . The construction began in 2003 and finished in 2008. Table 1 shows the basic specification of these two dams.

**Table 1.** Details about Xiaowan Dam and Jinghong Dam [27].

	Xiaowan	Jinghong
Surface area (km <sup>2</sup> )	$11.33 \times 10^4$	$14.91 \times 10^4$
Average annual inflow (m <sup>3</sup> · s <sup>-1</sup> )	1220	1840
Average annual discharge (m <sup>3</sup> )	$385 \times 10^8$	$580 \times 10^8$
Normal water level (m)	1240	602
Downstream water level (m)	991	538.5
Total storage (m <sup>3</sup> )	$153.0 \times 10^8$	$14.0 \times 10^8$
Dead storage (m <sup>3</sup> )	$43.5 \times 10^8$	$8.1 \times 10^8$
Annual generation capacity (kW × h)	$199.6 \times 10^8$	$73.4 \times 10^8$

Since WL measurements using RS imageries developed in this study requires a clear water extent variation, a selected boundary at each site covering the part close to the dam was used with obvious WA expansion after construction. Figure 3 shows the location and range of study area. Xiaowan Dam is the northernmost dam whose reservoir includes the mainstem of MR and the Heihui River, a major tributary in Yunnan Province. By comparing satellite images before and after impoundment, the WA with clear expansion can be identified. River channel used to estimate WL for Xiaowan Dam is shown as red area in Figure 3a. Two Envisat passes, #97 and #190, have crossovers near the dam. However, both passes within steep terrain are not able to generate successful height estimates due to severe waveform contamination. We instead only chose Jason-2 ground track #140 that had more stable performance over narrow river, the altimetry observed WL appears to be more accurate.

For Jinghong Dam, the river channel used for WA–WL conversion is displayed as red area in Figure 3b. This area has covered almost of the entire reservoir with a distance to the Nuozhadu Dam upstream of ~18 km. The water surface is intersected by two Envisat passes, #97 and #147, but no Jason-2 ground track is available. We later chose #97 as our data source since pass #147 also suffered from serious land contaminations that caused the retrieval of WL to be impossible. For the other four check points downstream of Jinghong Dam, D1 is near Envisat pass #362 and Jason-2 #103; D2 is a connection between Envisat #54 and Jason-2 #140; D3 has Envisat #283 and Jason-2 #179; and D4 is covered by Jason-2 #140.

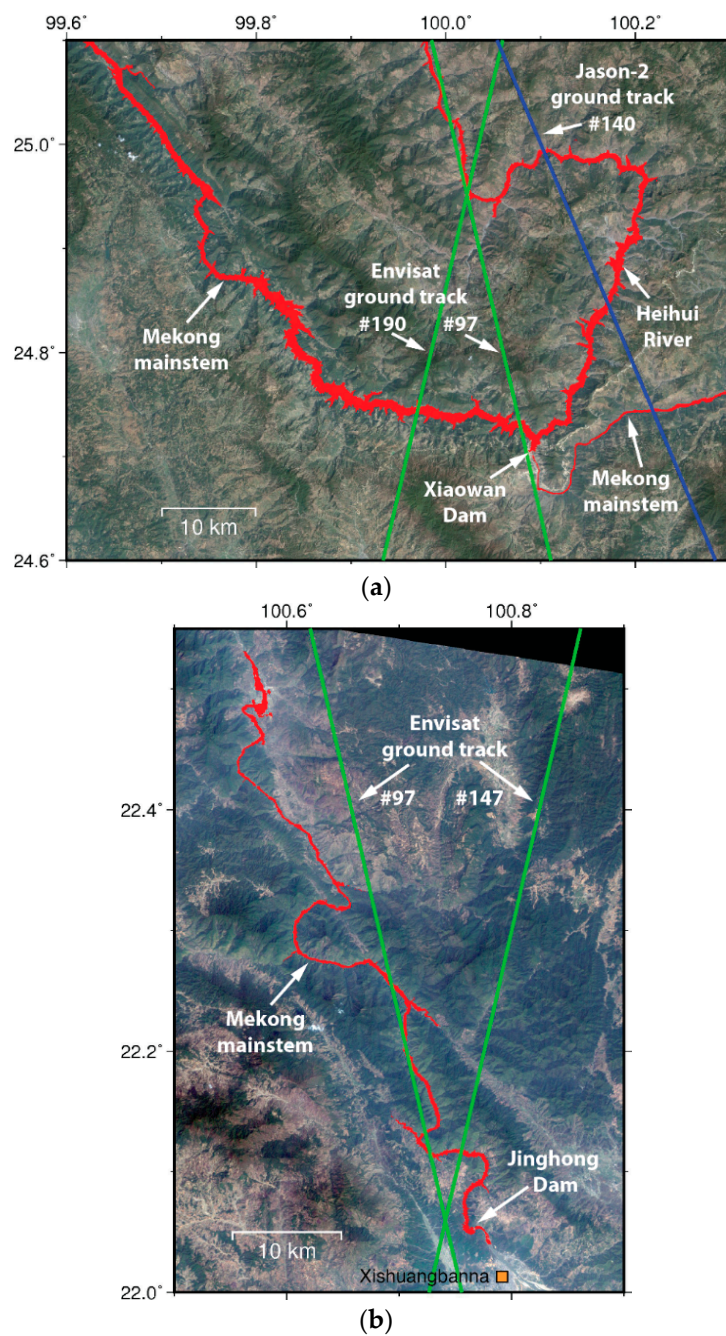


**Figure 3.** Extracted water surface (red area) of: (a) Xiaowan Dam after impoundment; and (b) Jinghong Dam after impoundment. The background images are composed by Landsat-7 natural color combination (RGB: band 3, 2, 1). Envisat and Jason-2 ground tracks are denoted by green and blue lines, respectively.

### 3. Data and Methodology

The data used in the study include multi-mission satellite RA (Envisat and Jason-2) measurements, Landsat optical satellite imagery and a DEM. The workflow from data collection and processing to WL time series construction is shown in Figure 4. The impact of these dams to the midstream and downstream is further assessed, and the contribution due to rainfall anomaly is discussed.

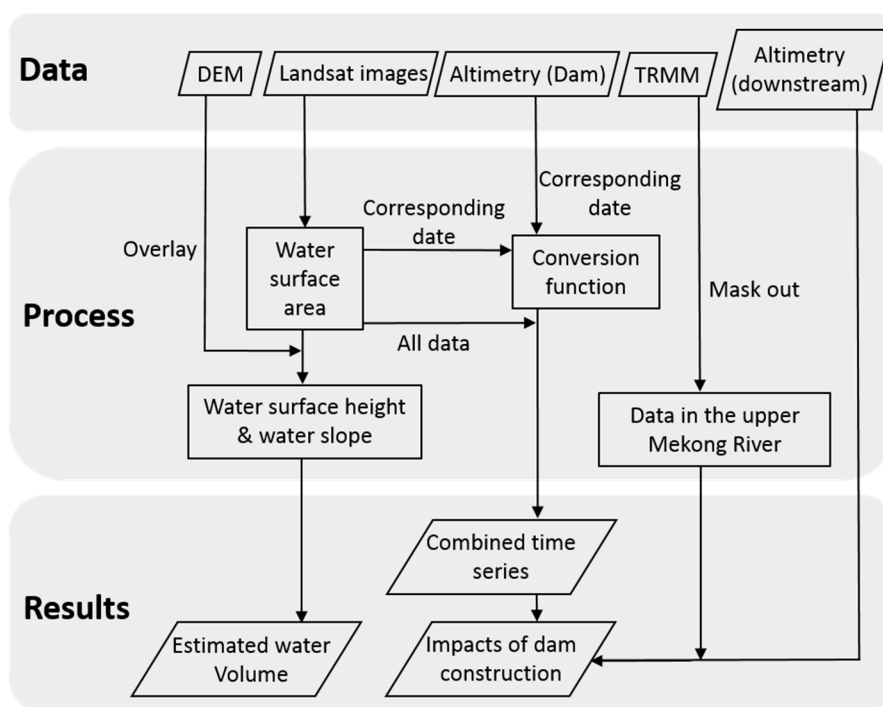


**Figure 4.** Flowchart of the methodology developed in this study.

### 3.1. Satellite Radar Altimetry

Satellite RA was originally designed to map global sea surface topography. A series of altimetry missions have been operated or operating in space, such as NASA's Seasat, Geosat, TOPEX/Poseidon, Jason-1/-2, European Space Agency's (ESA) ERS-1/-2, Envisat, Cryosat-2, the SARAL/AltiKa mission jointly operated by CNES and the Indian Space Research Organization (ISRO), and the recently launched Jason-3 and Sentinel-3A missions. The basic principle is that satellite altimetry sends an electromagnetic pulse to the nadir point of the satellite and receives the reflected signal coming from water or other surfaces. In an ideal condition, by calculating the two-way travel time of radar pulses, the distance between the satellite and mean surface covered by a circular footprint (3–5 km in radius [28,29]) can be derived and further converted into surface height measurement. In practical application, there are several correctional terms need to be considered in the computation. For example, the medium effect (ionosphere and troposphere delay), surface tidal signal (pole tide and solid earth tide), instrument errors (Ultra Stable Oscillator; distance between satellite mass center and receiver phase center), and orbit errors. After that, the waveform retracking algorithm is applied to locate the midpoint of leading edge to determine time elapse for range estimation. Over the ocean, the Brown model [30] is preferred to fit the waveform with physical parameters. For other surface types, such as ice sheet and inland water bodies, a suite of waveform retracking algorithms are developed to satisfy the unique pattern of the waveform from each kind of surface types.

In this study, Jason-2 and Envisat radar altimetry data were utilized to obtain WL at river crossovers. Envisat, a follow-on mission after ERS-1/-2 that was launched by ESA in 2002 and decommissioned in 2012, has a 35-day repeat period with an inclination of 98.5°. The inter-track distance at the Equator is about 80 km [31]. It was equipped with a dual frequency radar altimeter working in Ku and S bands. In 2010, it was maneuvered to a decreased orbital height, which no longer followed the same repeat cycle and ground tracks. Therefore, only high frequency (18 Hz) Ku-band data in the regular operation mode during 2002–2010 were used in this study. The altimetry data are stored in Sensor Geophysical Data Records (SGDRs) format for each cycle. The parameters include satellite position and timing, distance between satellite and surface and corrections. The Envisat SGDRs

contained four different ranges calculated by standard waveform retracking algorithms, including Ocean [30], ICE-1 [32,33], ICE-2 [34] and SEAICE [35]. ICE-1 retracker was originally developed for ice sheet observation purposes. The waveform over inland waterbody with specular shape is similar to the return from ice sheet. Therefore, ICE-1 retracker is suitable in the study to calculate range measurements.

For Xiaowan Dam, the construction finished after 2010 and the original river channel is too narrow to be detected. Jinghong Dam finished in 2008 was able to be observed by Envisat pass #97, which has ~500 m water crossover. In order to ensure waveforms that were reflected from the water surface, a 15 dB backscattering coefficient (BC) threshold was set. The BC is used as an indicator of surface roughness, the higher the BC and flatter the surface in general [22]. Hence, BC lower than 15 dB is considered to be other objects on the ground. After applying correctional terms and waveform retracking adjustment, the altimetry WL time series near Jinghong Dam is created.

Ocean Surface Topography Mission (OSTM)/Jason-2 was launched in 2008. It is a follow-on mission to the TOPEX/Poseidon and Jason-1 missions. Jason-2 is equipped with a Ku/C-band dual-frequency radar altimeter that produces a sampling rate at 20 Hz, corresponding to a ground interval at 330 m. In previous studies, Jason-2 can detect narrower river channel compared with previous altimeters, primarily because of its higher Pulse Repetition Frequency (PRF) at 2060 Hz [36,37], higher than Envisat (1795 Hz) [38]. The orbital design of Jason-2 has a revisiting cycle at every ten days while the tradeoff is a wider inter-track distance at 310 km. Over the MR basin, Xiaowan Dam can be observed by Jason-2, but Jinghong Dam has no crossovers within the reservoir. We used a similar 15 dB BC to ensure footprints were reflected from the water surface.

### 3.2. Optical Remote Sensing Imageries

Satellite optical imagery (e.g., Landsat) has been shown powerful in characterizing the water-surface dynamics of inland water bodies [39–41]. In this study, Landsat-5/-7/-8 images were used to retrieve WA measurements. Landsat-5 carried the Thematic Mapper (TM) sensor, and the mission life covered from 1984 to 2012. Landsat-7 has the Enhanced Thematic Mapper Plus (ETM+) onboard, covering 1999 to present. Both satellites have a 30 m spatial resolution and 16-day repeat cycle. Both TM and ETM+ images have eight spectral bands ranging between visible and mid-infrared (MIR) wavelengths. Landsat-8 carries two instruments, including the Operational Land Imager (OLI) and the Thermal Infrared Sensor (TIRS), to monitor the Earth's surface through passive microwave radiometry. In the study, OLI images were used to extract water surface. OLI contains refined heritage bands and three other new bands, deep blue (also called coastal/aerosol band), an additional shortwave infrared and quality assessment band. The spatial resolution of OLI image is 30 m, and the temporal resolution is 16-day with an 8-day offset from Landsat-7. The sampling rate and combined time span should potentially be a good complement to altimetry data.

All the available Level 1 image products were downloaded from U.S. Geological Survey (USGS) EarthExplorer website [42]. Images were stored in GeoTiff format. For each study area, clear images without cloud cover over river channel were selected. The Digital Numbers (DNs) in each Landsat-5/-7 image were then converted into Top-of-Atmosphere (ToA) reflectance using Equations (1) and (2) [43].

$$L_{\lambda} = gain \times DN + bias \quad (1)$$

$$\rho_{\lambda} = \pi \times L_{\lambda} \times d \times ESUN_{\lambda} \times \cos\theta_s \quad (2)$$

where  $L_{\lambda}$  is the cell value as radiance, DN is the cell value digital number, gain is the gain value for a specific band, bias is the bias value for a specific band,  $\rho_{\lambda}$  is the unitless planetary reflectance (ToA reflectance),  $d$  is the Earth–Sun distance in astronomical units,  $ESUN_{\lambda}$  is the mean solar exoatmospheric irradiances, and  $\theta_s$  is the solar zenith angle.

For Landsat-8 image, the conversion follows equations shown below [44]:

$$\rho\lambda' = M_{\rho}Q_{cal} + A_{\rho} \quad (3)$$

where  $\rho\lambda'$  is the ToA planetary reflectance without correction for solar angle,  $M_{\rho}$  is the band-specific multiplicative rescaling factor,  $A_{\rho}$  is the band-specific additive rescaling factor, and  $Q_{cal}$  is the quantized and calibrated standard product pixel values (DN). Furthermore, the ToA reflectance with a correction for the sun angle is:

$$\rho\lambda = \frac{\rho\lambda'}{\sin(\theta_{SE})} \quad (4)$$

where  $\rho\lambda$  is the ToA planetary reflectance and  $\theta_{SE}$  is the local sun elevation angle.

The WA extraction for Landsat TM/ETM+ imageries can be achieved by several matured algorithms, such as single band estimation [45], depending on the complexity of surrounding surface types. In this case, a more robust method namely the Modified Normalized Difference Water Index (MNDWI) using green and mid-infrared bands was applied to extract water [46]. In spectral analysis, waterbody has a strong reflectance in green band and substantial absorption in mid-infrared band. MNDWI is thus used to enhance this pattern to delineate water feature from other ground objects. The calculation of MNDWI is showed in Equation (5):

$$\text{MNDWI}_{\text{Landsat}} = \frac{\text{Green} - \text{MIR}}{\text{Green} + \text{MIR}} \quad (5)$$

where Green is the Landsat-5/-7 TM/ETM+ band 2 at 520–600 nm and MIR is band 5 at 1550–1750 nm. Due to a band shift, Green indicates Landsat-8 OLI band 3 at 530–590 nm and MIR is band 6 at 1570–1650 nm.

The MNDWI threshold is slightly different for each study area. For TM/ETM+, the value 0.2 was set at the beginning and iterated between 0.15–0.3 with an increment of 0.01 to find the best result. By inspecting several locations with false color images and testing different threshold values, a threshold equal to 0.23, which provided the most accurate result compared with waterbody in the original images, was selected for our study areas. For OLI images, because the bandwidth of OLI in MIR is much narrower than TM/ETM+, the OLI band 6 images will be darker than TM/ETM+ band 5 images, leading to higher MNDWI values at waterbodies. The narrower bandwidth also causes sensitive MNDWI variation, meaning a slight change of threshold would alter classification result. Therefore, a different threshold at 0.4 was set for classification. Moreover, to avoid potential noise caused by clouds and terrain shadows, a river channel after impoundment plus a 5-pixel buffer area was used as a mask to further constrain the water extent. Samples of extracted WA in Xiaowan and Jinghong Dams are shown in Figure 3.

### 3.3. Digital Elevation Model (DEM)

DEM provides a good reference for surface elevation during the time when airborne or spaceborne sensors compiled the height in each grid. Shuttle Radar Topography Mission (SRTM) is one of the most commonly used global DEMs in RS studies. It obtained the topography by the Space Shuttle Endeavour using C-band radar interferometry in 2000. The data product used here is version 2 with global 90 m resolution, covering 60°N–56°S, which includes the upper Mekong stream [47]. The vertical uncertainty of SRTM DEM in mountainous area is about 10 m [48]. Because data acquisition is earlier than the construction of these two dams, it is suitable to estimate WV changes after impoundment. SRTM was used to provide information about the bathymetry (above old river surface) of entire reservoir. The computation is to simply accumulate WV in each grid, from an elevation of DEM up to the elevation of water mask given by Landsat imageries.

### 3.4. Precipitation Record

Water budget (described by WA and WL) of the dams is controlled by the climate-driven hydrologic processes and precipitation is the most dominant one. Thus, analyses based on the precipitation data are conducted to evaluate the climate influence on the hydrology of dams. Due to the limited availability of the ground-based precipitation data in the upper MR basin, we have to rely on a space-borne meteorological satellite, *i.e.*, Tropical Rainfall Measuring Mission (TRMM, from the joint NASA and JAXA), to provide precipitation data for our study in this region. Launched in 1997 and decommissioned in 2015, the major task of TRMM was to collect rainfall data for tropical and subtropical cyclones, monsoon, and regional weather/climate research [49]. The payloads include a single frequency precipitation radar (PR), TRMM microwave imager (TMI), visible and infrared scanning radiometer (VIRS), clouds and the Earth's radiant energy sensor (CERES) and lightning imaging sensor (LIS). Combined all these observations and derived products, the precipitation amount over tropical and subtropical area was estimated, and had been demonstrated a reliable precipitation record in several past studies [50–52].

The precipitation dataset used in the study is the latest post-processed Version 7 of TRMM 3B43 [53]. It is a monthly mean precipitation of daily mean rainfall rate at  $0.25 \times 0.25$  degree resolution. Monthly mean precipitation of the study area was estimated based on the TRMM data covering the portion of Mekong basin from headwater until each check point, such as Xiaowan Dam, Jinghong Dam, and D1–D4. An annual mean precipitation rate was calculated by averaging the monthly values in a year while the anomaly of annual precipitation is based on the overall data record from 1998 to 2015. As a result, we have the opportunity to investigate the WA/WL variation in association with the precipitation anomaly.

In the study, the precipitation anomaly is derived to verify whether there is a decadal precipitation trend that may cause interannual WL variation in the MR. TRMM dataset has good quality to derive rainfall variation trend during a long time span [54].

### 3.5. Relationship between Water Level, Water Area and Water Volume

To construct a conversion function between WA and WL, we first selected satellite images that were temporally coincident with altimetry measurements. We assumed the images acquired within  $\pm 5$  days of altimetry data had the same WL for WA–WL conversion. It is worth noting that in these two study sites, we used a linear function to fit the relationship between WA and WL. This contains uncertainty while the terrain slope is not a constant within the interval of water variation, and causing various non-linear WL–WA relationships correspond to different river sections. However, it's impossible to create accurate conversion function that fit every river section. Hence, the mountainous terrain in our study area is assumed to have constant slope. The analysis results shown in Figure 5 indicate that the linear functions (Equations (6) and (7)) work well without significant bias and are able to describe the WA–WL relationships for the selected Dams.  $R^2$  (square of the Pearson correlation coefficient) between altimetry WL and RS-derived WA in both two study area are  $>0.95$ , which represent highly correlated relationship between WL and WA, and proved the linear regression is sufficient to generate conversion function for our study areas.

$$WL_{\text{Xiaowan}} (\text{m}) = WA_{\text{Xiaowan}} (\text{km}^2) \times 1.611 + 1034 \quad (6)$$

$$WL_{\text{Jinghong}} (\text{m}) = WA_{\text{Jinghong}} (\text{km}^2) \times 2.549 + 491.3 \quad (7)$$

The next step is to estimate WV based on WA. We overlap the extracted WA and DEM layers, and calculate the WV above the DEM by integration of column water. Similarly, a linear regression approach is applied to derive the relationship between WV and WA. For example, Equation (8) has been derived to describe the WA–WV relation of Jinghong Dam.

$$WV_{\text{Jinghong}} (\text{km}^3) = WA_{\text{Jinghong}} (\text{km}^2) \times 2.76 \times 10^7 + 6.95 \times 10^7 \quad (8)$$

The transfer functions above (Equations (6)–(8)) allow seamless conversion among the WA, WL and WV variables and make it possible to extend the WL and WV estimation to the times even one of WL or WA is not available.

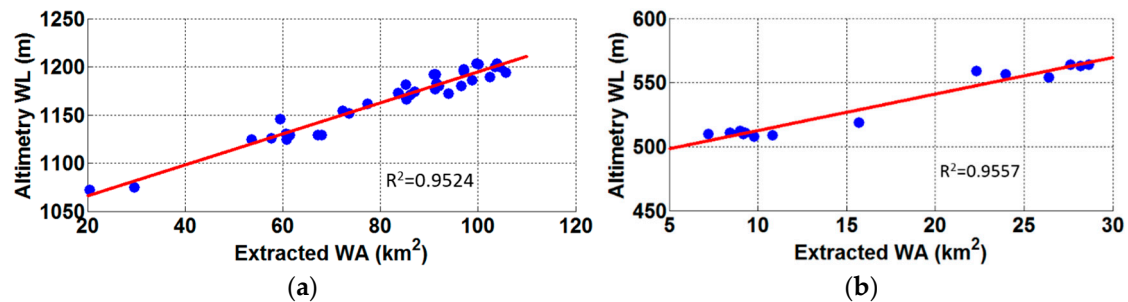


**Figure 5.** Relationships between WL and WA of: (a) Xiaowan Dam; and (b) Jinghong Dam. Blue points: Coincident WL and WA measurements (acquired within five days). Red line: linear regression of blue points.  $R^2$ : R square between WL and WA.

## 4. Results

### 4.1. Time Series from Multiple Sensors

WL observed by combined altimetry and RS imageries in Xiaowan and Jinghong Dams are shown in Figure 6a,b, respectively. Four downstream crossovers specified in Figure 2 (D1–D4) are shown in Figure 6c–f. In Figure 6a,b, an increased WL during impoundment of each Dam can be clearly identified from the time series. For Xiaowan Dam (Figure 6a), the impoundment was mainly separated into three stages, during 2009–2013, with a total rise of WL about 140 m. For Jinghong Dam (Figure 6b), the impoundment happened in early 2008. The pattern of impoundment is clearly seen by radar altimeter and the WL anomaly matches pretty well with local reports, both in time and in amplitude. In Figure 6a,b, seasonal WL variation can also be observed by Landsat imageries and altimetry satellites, during either constructing or operating phase of the Dams. These two independent observations with distinct sensing approach correlated very well during the overlapping period. The RS data clearly serves as the supplemental observation that lengthens the time series towards multi-decadal coverage.

It is worth noting that for RS imageries, cloud cover, and terrain effect resulted in increased error or failure in WL retrieval, especially in wet seasons. The time series given by RS imageries has lower sampling rate than nominal 16-day and even just a few samples in a year, such as 2011 and 2012 for Jinghong Dam (panel b). Based on the limitation inherent in optical RS, the Landsat images along cannot be a self-sustaining source to produce regular and frequently sampled time series, particularly in this demonstrated area. However, it is obvious that the extra measurement given by RS imageries is complementary to radar altimetry. It helps to detect exceptional changes in the waterbody, and the spatial coverage is almost unlimited around the world. Further discussions about Figure 6c–f will be shown in Section 4.4, which focuses on the impact to downstream locations.

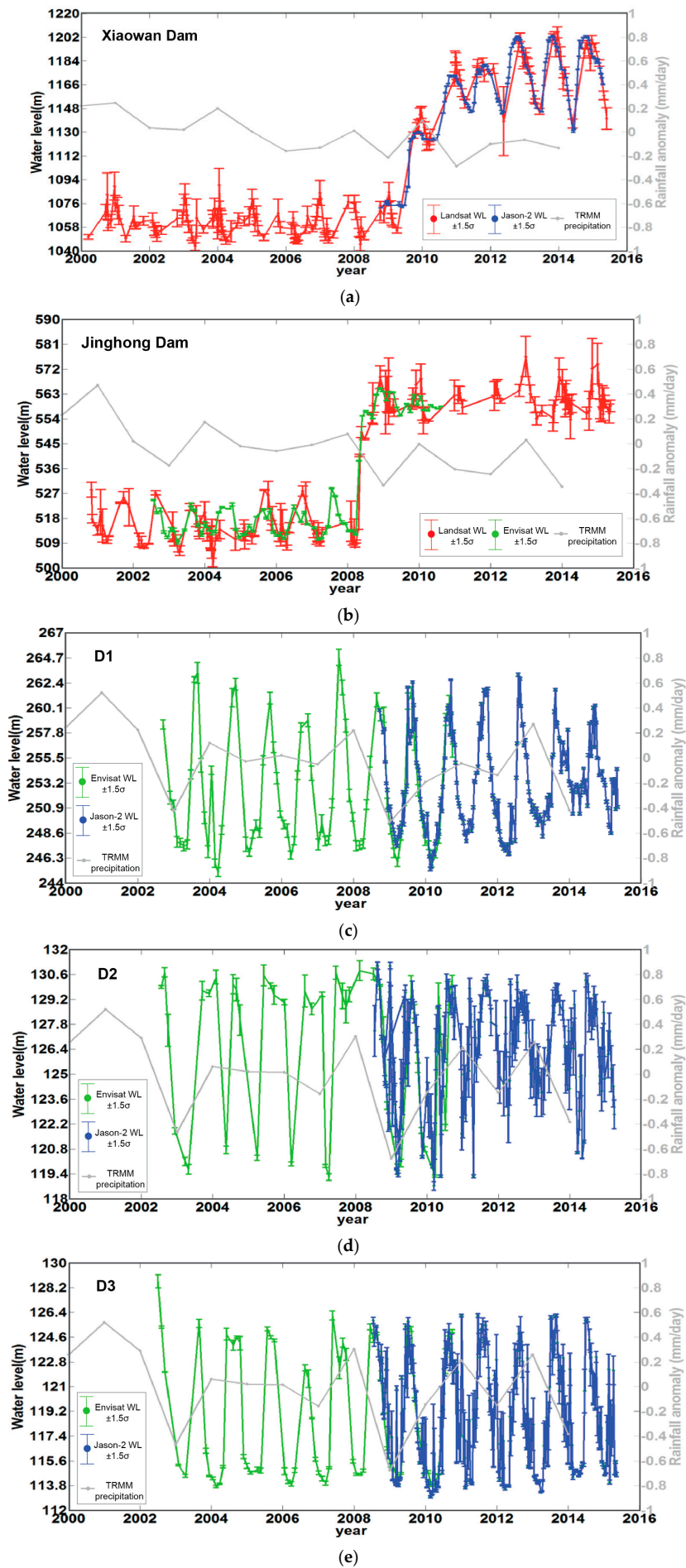
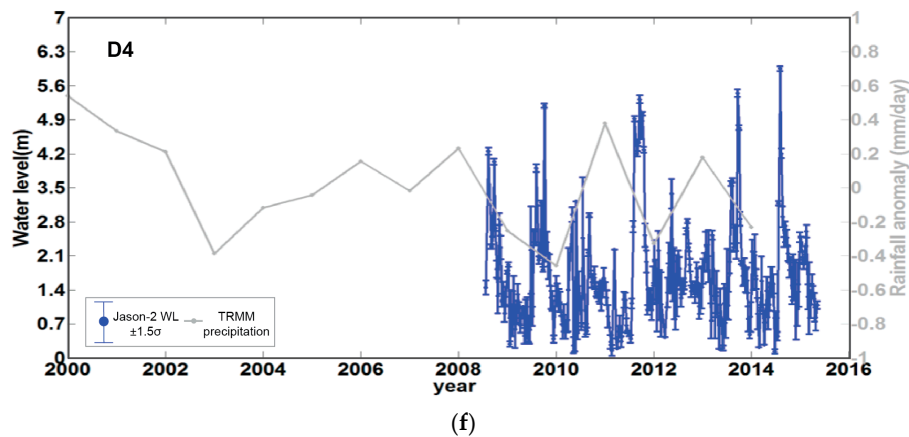


Figure 6. Cont.



**Figure 6.** Time series of rainfall rate anomaly and WL measured by multiple sensors at: (a) Xiaowan Dam; (b) Jinghong Dam; and (c–f) the four measurement sites in the downstream (D1–D4, Figure 2). The red broken line in all panels is the measurement from RS images, the blue line is from Jason-2, and the green line is from Envisat. These WL estimates, regarding WGS84 ellipsoidal height, refer to the left ordinate in meter. There is also annual rainfall rate anomaly plotted as gray line shown in the background of each panel, which refers to the right ordinate. Positive (negative) anomaly values means the precipitation of that year is more (less) than the long-term average rainfall rate.

#### 4.2. Validation at Xiaowan Dam

Due to the lack of gauge data, we collected several WLs from local news during each stage of construction in Xiaowan Dam. The available ground truth is not routinely reported and only available before and after the impoundment. It should be emphasized that the datum used for these announced water elevations also remain elusive. However, since the numbers quoted in the news basically released by the local agency that operated the hydropower station (such as China Huaneng Group), it is appropriate to assume the datum is the same for announced numbers. Hence, the WL changes can be used to compare with satellite measurements. The standard deviation of reported WL and estimated WL derived from a combination of altimetry and Landsat-derived measurements is 5.92 m during the five different time periods as shown in Table 2.

**Table 2.** Comparison between local water level information and estimated results of Xiaowan Dam.

	20 July 2009	15 August 2009	1 August 2010	9 August 2011	15 November 2011	31 October 2012
<b>Local data (m)</b>	1085	1126	1146	1173	1178	1200
<b>Estimate results (m)</b>	1084.78	1116.27	1144.46	1180.92	1181.68	1201.48

#### 4.3. Validation at Jinghong Dam

The local information of Jinghong Dam is obtained from Mekong River Commission website [8]. However, the announced data only covered wet seasons from 2009 to 2015. Only a few corresponding values could be compared due to cloud cover in wet seasons. The timing and WL estimates provided by gauge data and RS approach is shown in Table 3. The standard deviation of the difference between satellite-derived WL and ground truth is about 1.13 m for these six points.

By comparing Tables 2 and 3, it is noted that the discrepancy of estimated water level is larger in Xiaowan Dam than in Jinghong Dam. This is mainly because the dates used for comparison, 2009–2012, is the timing when Xiaowan Dam was experiencing three steps of water impoundment. Satellite-derived WL and *in situ* data may have inconsistency within the five-day assumption made in Section 3.5. Assuming the WL increasing rate stayed linear between first date (20 July 2009) and second date (15 August 2009) in Table 2, a five-day difference may result in ~8 m of WL difference. In contrast,

Jinghong Dam during the same period had only seasonal variability, which better demonstrates the actual accuracy of the satellite-derived WL.

**Table 3.** Comparison between gauge data and estimated results of Jinghong Dam.

	22 June 2009	31 August 2009	5 October 2009	12 July 2010	16 August 2010	23 September 2012
<b>Gauge data (m)</b>	555.77	560.36	557.05	556.91	556.88	557.45
<b>Estimate results (m)</b>	555.08	559.44	556.29	557.66	558.5	558.68

The WLs before and after impoundment are also compared in Table 4, where the information is obtained from navigation information of transportation [55]. Due to the issue of datum difference, this comparison only focused on water level change at the dam. Both local information and estimate results showed that impoundment height is about 50 m.

**Table 4.** Comparison of impoundment height of Jinghong Dam.

	Before Impoundment	After Impoundment	Difference
<b>Local information (m)</b>	544.9	602	57.1
<b>Estimate results (m)</b>	510	560	50

The WV is also calculated in Jinghong Dam. The estimated WV by integrating column water from SRTM surface elevation to the elevation given by RS water mask is  $8.38 \times 10^8 \text{ m}^3$  on 9 March 2009 (dry season). The number is close to the nominal dead storage of Jinghong Dam at  $8.1 \times 10^8 \text{ m}^3$  [27], containing an error about 3%.

#### 4.4. Impact of Downstream Hydrologic Schemes

Four selected downstream cross points, including Jason-2 and Envisat altimetry data, were utilized to measure WL before and after the Dam operations. These four points were named D1, D2, D3, and D4 from upstream to downstream, as specified in Figure 2. The distance between D1 and D2 is about 550 km, and about 110 km between D2 and D3. D4 is the most downstream checkpoint, located in Cambodia and approaching the river outlet. By inspecting WL at D1 and D2 immediately following Jinghong Dam, shown in Figure 6c,d, the annual lowest WL appears an increasing trend after Jinghong Dam's operation in 2008. In the meantime, the highest WL every year also faces a trialing tendency after 2008, especially after 2012 when Xiaowan Dam was put into service. By examining the annual precipitation rate anomaly in Figure 6, the time series varies between  $\pm 0.5 \text{ mm} \cdot \text{day}^{-1}$  within upper MR watershed in the last decade. By assuming a homogeneous and steady evaporation, we may presume the upper MR has a stable water input since 2008. Thus, we consider that the trend of WL is less correlated and influenced by local precipitation when we analyzed the historical TRMM data set. Among all factors, water storage regulation in a cascade of dams in the upstream is speculated to create such an enormous momentum in WV changes.

From Figure 6a,b, we confirmed that the impoundment of Xiaowan and Jinghong Dam was only executed in wet season, and the impacts to downstream were not significant at the time of impoundment in 2008. We investigated some local news and reference papers that informed several flood events after 2008. For example, the situation report released by Cambodia Humanitarian Response Forum (HRF) [56] indicates a flood event stroke Cambodia in 2013. There is also an article that mentions two flood events occurred in 2008 and 2011 [57]. These flood events can be seen at location D4 in Figure 6f. However, based on our analysis these events were more likely caused by anomalous precipitation indicated by gray line in Figure 6f. The WLs at D1–D3, near the midstream of MR, had no exceptional rise in those years.

We calculated the mean WL in wet seasons (May–October) and dry seasons (January–April and November–December) for D1–D4 in each year. Then, we applied a linear regression to derive the WL trend for each specified season. Because Jinghong Dam finished the impoundment in the first half of 2008, as seen in Figure 6b, years used to compute wet season trend covering 2008–2015. However, dry season in early 2008 is not affected by the dams and should be excluded in the analysis. Therefore, we selected dry seasons from 2009 to 2015 and derive the annual change to focus on the impact of Dam operations. The results of each cross point, D1–D4, are shown in Figure 7. The uncertainty of WL estimate, as computed from  $2\text{-}\sigma$  of data points in each season, is denoted as error bar in Figure 7.

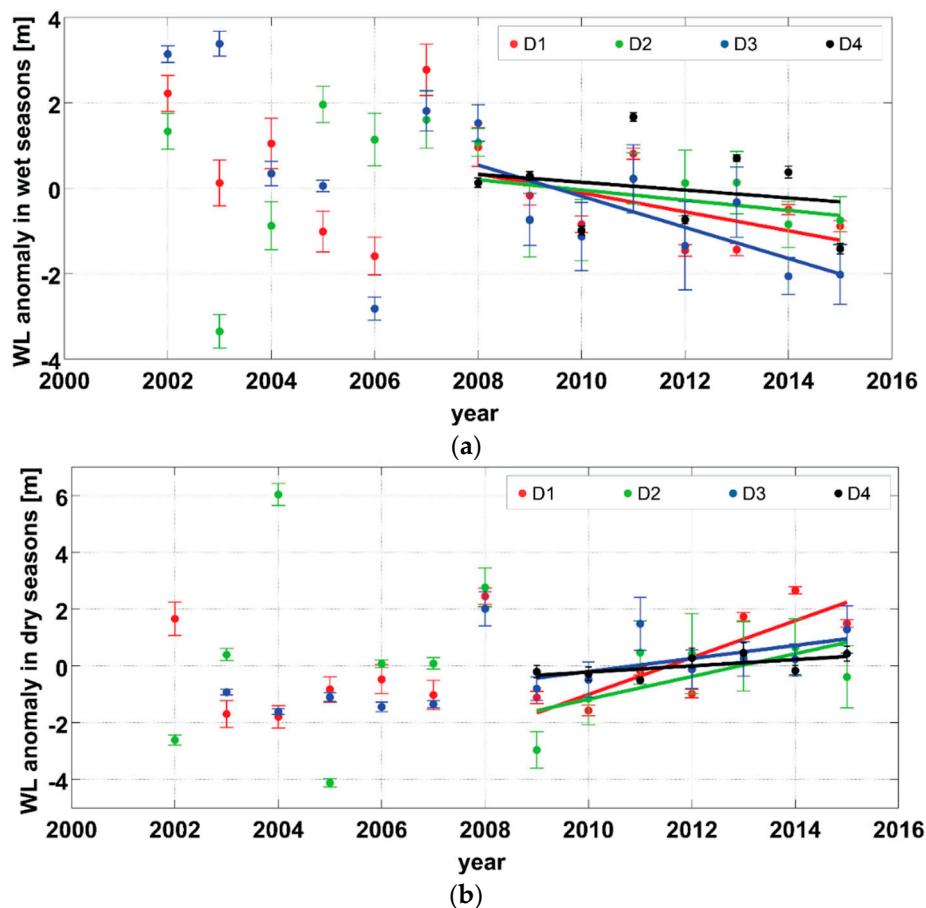


**Figure 7.** (a) A decreasing trend of mean WL in wet seasons from 2008–2015. The measurements have been removed the mean itself for comparison. (b) An increasing trend of mean WL in dry seasons from 2009–2015 for D1–D4.

Based on the results of Figure 7, rate of trend at each point is summarized in Table 5. For D1–D4, the average decreasing rate of maximum WL is about  $0.20 \text{ m} \cdot \text{year}^{-1}$ , and the average increasing rate of minimum WL is about  $0.35 \text{ m} \cdot \text{year}^{-1}$ . We conclude that the impoundment of these dams has reallocated water resources and changed river flow patterns compared with earlier years. Our results support the simulation in [5] that mostly relied on hydrological models.

**Table 5.** Trend of average WLs in defined wet (dry) seasons at downstream locations. Unit: ( $\text{m} \cdot \text{year}^{-1}$ ).

	D1	D2	D3	D4	Mean (D1–D4)
Wet seasons	−0.22	−0.12	−0.36	−0.09	−0.20
Dry seasons	0.65	0.40	0.23	0.11	0.35

Meanwhile, the pattern of shrinking water variability also seems to be less clear at point D4, which is distant from these dams. From the dry season WL variation rate in Table 5, the closer to the dams, the larger increasing WL rate. It is suspected that along with the distance to the dams, water sources coming from other tributaries compensate the man-made adjustment and the pattern becomes insignificant. The influence of natural events (monsoon and storms) would dilute the WL variation pattern. Additionally, a reference paper [58] mentions about two drought events happened in 2009 and 2010, which can be identified in Figure 6c–e by lower WL than other years. Therefore, some of the extreme WL variation may not be caused by the Dam operations but nature effects. The long-term trends shown in Figure 7a,b, on the other hand, are more likely caused by the dam construction.

## 5. Discussions

In this study, we investigated the hydrologic changes in the downstream of MR as a consequence of Dam operations upstream. Both RA and RS imageries can detect the impoundment of Xiaowan and Jinghong Dams. The WV estimates based on DEM and MNDWI imageries also agree well with *in situ* data. However, some issues still need to be resolved or improved for further research. First, the extracted WA still contains errors due to terrain and cloud effects. In the future, it is preferred to establish a comprehensive decision tree for water delineation to exclude pixels with similar spectral behavior. Second, the conversion functions in current study were derived from first-order linear regressions, but the topography of the dams is not a linear structure. Formation of terrain should be taken into account to improve the estimates of empirical relationships between water extent and WL variations.

From precipitation perspective, except for normal variability in the annual signal, it is observed a slight downward trend from 2009 to 2015, which is arguably caused by regional climate change [58]. This phenomenon, although gradual, perhaps affects WL variation at the downstream area and requires a longer term observation to quantify the impact. In this study, the data source is monthly mean rainfall with coarser spatial resolution. It is suggested to utilize daily data that could obtain sudden and intensifying rainfall that has been averaged out in current data. Moreover, the melting glacier in the upper Mekong watershed could also contribute to the water level variations. It is necessary to quantify the freshwater storage changes of these mountain glaciers and exclude them from our impact analysis. Finally, as mentioned before, the rates of evaporation and runoff could vary and cause uncertainty in the water budget as well.

More altimetry satellites are expected to facilitate our future work on this topic, including Jason-3 (launched on 17 January 2016), Sentinel-3 two-satellite constellation (16 February 2016), Jason-CS/Sentinel-6 (2020) and Surface Water and Ocean Topography (SWOT) (2020). These and other new-generation satellites with improved designs of hardware will potentially outperform those historical missions. For example, the single band radar altimeter onboard SARAL/AltiKa used Ka-band radar pulse to minimize the interference of ionosphere delay of radar range. Cryosat-2, Sentinel-3, and Jason-CS carried or will carry the delay-Doppler altimeter, or the SAR altimeter to further partition the radar footprint into narrow bands in cross-track direction, and thus increase ground resolution in along track direction. SWOT is a wide-swath interferometric altimeter also with a nadir Ka-band altimeter that would improve the spatial resolution of the WL measurements to 100 m.

For optical satellite images, based on the well-correlated results at Xiaowan and Jinghong Dam, we expect to further integrate the WA measurements at downstream sections with nearby *in situ* data provided by MRC, and create conversion function. For some gauge stations, the *in situ* data only covered a short period, which is not enough for long-term analysis. Additionally, gauge WL observation has high accuracy and dense sampling rate, suitable to generate high quality conversion function. Once we create conversion function for a particular region, the continuous and extended WL time series can thus be generated through numerous optical satellite images.

## 6. Conclusions

In this paper, we demonstrated an effective monitoring system to observe basin-scale WL variations by integrating data from multiple satellite observations. Two reservoirs and four river crossovers covered by altimetry and optical RS satellites were analyzed to study the WL changes since the operations of dams in the upper Mekong basin. A decreasing trend in wet seasons and an increasing trend in dry seasons is identified by the combined time series. For now, the accuracy of estimated WL is limited to meter level, which might not suffice accurate hydrologic studies. However, this technique is promising because of its capability of densifying and extending the observations of WLs on remote rivers, lakes, and reservoirs, especially the monitoring of episodic signals such as dam water impoundment processes. It is expected that the sampling rate can be increased, and the temporal coverage can be widened using higher temporal/spatial resolution satellite imageries, from platforms such as Formosat-2 and SPOT series of optical or synthetic aperture radar satellites. It is possible to achieve daily WL observation by combining all these satellites except for cloud covers. In summary, due to the availability of a variety of optical imageries, the monitoring system developed in this study can be a valuable tool for the monitoring of surface water variations at adequately fine spatial scales for water resources management.

**Acknowledgments:** This work was supported in part by the Ministry of Science and Technology (MOST), Taiwan, under project 104-2119-M-008-005-MY2 and 104-2221-E-008-099-MY3, in part by the National Central University New Faculty Research Award. The Ohio State University component of the research is partially funded by NSF via the Belmont Forum/IGFA Grant (No. ICER-1342644). Chungyen Kuo was also partially supported by the Headquarters of University Advancement at National Cheng Kung University, Taiwan. We thank NASA, ESA, and CNES for providing the radar altimeter data, and NASA and USGS for providing the Landsat data used in this study.

**Author Contributions:** Kuan-Ting Liu and Kuo-Hsin Tseng are the primary authors who established the concept of the presented study. They performed the usage of remote sensing data including Landsat time series analysis to assess the impact of dam operations. C.K. Shum, Yuanyuan Jia, and Kun Shang advised on data processing methodologies, and helped interpret the results. Chian-Yi Liu performed TRMM data analysis and collected meteorological information at the study site. Chung-Yen Kuo and Ganming Liu were responsible for extracting altimetric height from Envisat and Jason-2 data record. All authors proofread the manuscript.

**Conflicts of Interest:** The authors declare no conflict of interest.

## References

1. Kite, G. Modelling the Mekong: Hydrological simulation for environmental impact studies. *J. Hydrol.* **2001**, *253*, 1–13. [[CrossRef](#)]
2. The GMT Home Page. Available online: <http://www.soest.hawaii.edu/gmt/> (accessed on 26 April 2016).
3. Wessel, P.; Smith, W.H. Free software helps map and display data. *Eos Trans. Am. Geophys. Union* **1991**, *72*, 441–446. [[CrossRef](#)]
4. Mekong River Commission. Strategic Environmental Assessment of Hydropower on the Mekong Mainstream. Available online: <http://www.mrcmekong.org/assets/Publications/Consultations/SEA-Hydropower/SEA-FR-summary-13oct.pdf> (accessed on 22 April 2016).
5. Räsänen, T.A.; Koponen, J.; Lauri, H.; Kumm, M. Downstream hydrological impacts of hydropower development in the Upper Mekong Basin. *Water Resour. Manag.* **2012**, *26*, 3495–3513. [[CrossRef](#)]
6. China's Upper Mekong Dams Endanger Millions Downstream. Available online: <https://www.internationalrivers.org/files/attached-files/03.uppermekongfac.pdf> (accessed on 22 April 2016).
7. International Rivers. Available online: <https://www.internationalrivers.org/> (accessed on 26 April 2016).
8. Mekong River Commission. Available online: <http://www.mrcmekong.org/> (accessed on 26 April 2016).
9. Fu, L.L.; Smith, R.D. Global ocean circulation from satellite altimetry and high-resolution computer simulation. *Bull. Am. Meteorol. Soc.* **1996**, *77*, 2625–2636. [[CrossRef](#)]
10. Siegel, D.A.; McGillicuddy, D.J.; Fields, E.A. Mesoscale eddies, satellite altimetry, and new production in the Sargasso Sea. *J. Geophys. Res.* **1999**, *104*, 359. [[CrossRef](#)]
11. Shaw, P.T.; Chao, S.Y.; Fu, L.L. Sea surface height variations in the South China Sea from satellite altimetry. *Oceanol. Acta* **1999**, *22*, 1–17. [[CrossRef](#)]

12. Van der Veen, C.J. Interpretation of short-term ice-sheet elevation changes inferred from satellite altimetry. *Clim. Chang.* **1993**, *23*, 383–405. [[CrossRef](#)]
13. Ekholm, S.; Forsberg, R.; Brozena, J.M. Accuracy of satellite altimeter elevations over the Greenland ice sheet. *J. Geophys. Res.: Oceans (1978–2012)* **1995**, *100*, 2687–2696. [[CrossRef](#)]
14. Kouraev, A.V.; Semovski, S.V.; Shimaraev, M.N.; Mognard, N.M.; Légresy, B.; Remy, F. Observations of Lake Baikal ice from satellite altimetry and radiometry. *Remote Sens. Environ.* **2007**, *108*, 240–253. [[CrossRef](#)]
15. Ridley, J.K.; Partington, K.C. A model of satellite radar altimeter return from ice sheets. *Remote Sens.* **1988**, *9*, 601–624. [[CrossRef](#)]
16. Lee, H.; Shum, C.K.; Tseng, K.H.; Huang, Z.; Sohn, H.G. Elevation changes of Bering Glacier System, Alaska, from 1992 to 2010, observed by satellite radar altimetry. *Remote Sens. Environ.* **2013**, *132*, 40–48. [[CrossRef](#)]
17. Lee, H.; Shum, C.K.; Yi, Y.; Braun, A.; Kuo, C.Y. Laurentia crustal motion observed using TOPEX/POSEIDON radar altimetry over land. *J. Geodyn.* **2008**, *46*, 182–193. [[CrossRef](#)]
18. Kuo, C.Y.; Cheng, Y.J.; Lan, W.H.; Kao, H.C. Monitoring vertical land motions in southwestern Taiwan with Retracked Topex/Poseidon and Jason-2 Satellite Altimetry. *Remote Sens.* **2015**, *7*, 3808–3825. [[CrossRef](#)]
19. Berry, P.A.M.; Garlick, J.D.; Freeman, J.A.; Mathers, E.L. Global inland water monitoring from multi-mission altimetry. *Geophys. Res. Lett.* **2005**, *32*. [[CrossRef](#)]
20. Frappart, F.; Calmant, S.; Cauhopé, M.; Seyler, F.; Cazenave, A. Preliminary results of ENVISAT RA-2-derived water levels validation over the Amazon basin. *Remote Sens. Environ.* **2006**, *100*, 252–264. [[CrossRef](#)]
21. Deng, X.; Featherstone, W.E. A coastal retracking system for satellite radar altimeter waveforms: Application to ERS-2 around Australia. *J. Geophys. Res.* **2006**, *111*. [[CrossRef](#)]
22. Legresy, B.; Papa, F.; Remy, F.; Vinay, G.; van den Bosch, M.; Zanife, O.Z. ENVISAT radar altimeter measurements over continental surfaces and ice caps using the ICE-2 retracking algorithm. *Remote Sens. Environ.* **2005**, *95*, 150–163. [[CrossRef](#)]
23. Liu, G.; Schwartz, F.W.; Tseng, K.H.; Shum, C.K. Discharge and water-depth estimates for ungauged rivers: Combining hydrologic, hydraulic, and inverse modeling with stage and water-area measurements from satellites. *Water Resour. Res.* **2015**, *51*, 6017–6035. [[CrossRef](#)]
24. Michailovsky, C.I.; McEnnis, S.; Berry, P.A.M.; Smith, R.; Bauer-Gottwein, P. River monitoring from satellite radar altimetry in the Zambezi River basin. *Hydrol. Earth Syst. Sci.* **2012**, *16*, 2181–2192. [[CrossRef](#)]
25. Kuo, C.Y.; Kao, H.C. Retracked Jason-2 altimetry over small water bodies: Case study of Bajhang River, Taiwan. *Mar. Geod.* **2011**, *34*, 382–392. [[CrossRef](#)]
26. King, P.; Bird, J.; Haas, L. *The Current Status of Environmental Criteria for Hydropower Development in the Mekong Region: A Literature Compilation*; WWF-Living Mekong Programme: Morges, Switzerland, 2007.
27. Fan, H.; He, D.; Wang, H. Environmental consequences of damming the mainstream Lancang-Mekong River: A review. *Earth-Sci. Rev.* **2015**, *146*, 77–91. [[CrossRef](#)]
28. Connor, L.N.; Laxon, S.W.; Ridout, A.L.; Krabill, W.B.; McAdoo, D.C. Comparison of Envisat radar and airborne laser altimeter measurements over Arctic sea ice. *Remote Sens. Environ.* **2009**, *113*, 563–570. [[CrossRef](#)]
29. Durrant, T.H.; Greenslade, D.J.; Simmonds, I. Validation of Jason-1 and ENVISAT remotely sensed wave heights. *J. Atmos. Ocean. Technol.* **2009**, *26*, 123–134. [[CrossRef](#)]
30. Brown, G.S. The average impulse response of a rough surface and its applications. *IEEE Trans. Antennas Propag.* **1977**, *25*, 67–74. [[CrossRef](#)]
31. Zelli, C.; Aerospazio, A. ENVISAT RA-2 advanced radar altimeter: Instrument design and pre-launch performance assessment review. *Acta Astronaut.* **1999**, *44*, 323–333. [[CrossRef](#)]
32. Bamber, J.L. Ice sheet altimeter processing scheme. *Int. J. Remote Sens.* **1994**, *15*, 925–938. [[CrossRef](#)]
33. Wingham, D.J.; Rapley, C.G.; Griffiths, H. New techniques in satellite altimeter tracking systems. In Proceedings of the ESA 1986 International Geoscience and Remote Sensing Symposium (IGARSS'86) on Remote Sensing: Today's Solutions for Tomorrow's Information Needs, Zurich, Switzerland, 8–11 September 1986.
34. Legresy, B.; Remy, F. Surface characteristics of the Antarctic ice sheet and altimetric observations. *J. Glaciol.* **1997**, *43*, 265–275.
35. Laxon, S. Sea ice altimeter processing scheme at the EODC. *Int. J. Remote Sens.* **1994**, *15*, 915–924. [[CrossRef](#)]
36. Birkett, C.M.; Beckley, B. Investigating the performance of the Jason-2/OSTM radar altimeter over lakes and reservoirs. *Mar. Geod.* **2010**, *33*, 204–238. [[CrossRef](#)]

37. Dumont, J.P.; Rosmorduc, V.; Picot, N.; Desai, S.; Bonekamp, H.; Figa, J.; Scharroo, R. *OSTM/Jason-2 Products Handbook*; NOAA/NESDIS: College Park, MD, USA, 2009.
38. Resti, A.; Benveniste, J.; Roca, M.; Levrini, G.; Johannessen, J. The Envisat radar altimeter system (RA-2). *ESA Bull.* **1999**, *98*, 1–8.
39. Pietroniro, A.; Prowse, T.; Peters, D. Hydrologic assessment of an inland freshwater delta using multi-temporal satellite remote sensing. *Hydrol. Process.* **1999**, *13*, 2483–2498. [[CrossRef](#)]
40. Xu, H. Extraction of urban built-up land features from Landsat imagery using a thematic-oriented index combination technique. *Photogramm. Eng. Remote Sens.* **2007**, *73*, 1381–1391. [[CrossRef](#)]
41. Ko, B.C.; Kim, H.H.; Nam, J.Y. Classification of potential water bodies using Landsat 8 OLI and a combination of two boosted random forest classifiers. *Sensors* **2015**, *15*, 13763–13777. [[CrossRef](#)] [[PubMed](#)]
42. EarthExplorer. Available online: <http://earthexplorer.usgs.gov/> (accessed on 26 April 2016).
43. Chander, G.; Markham, B.L.; Helder, D.L. Summary of current radiometric calibration coefficients for Landsat MSS, TM, ETM+, and EO-1 ALI sensors. *Remote Sens. Environ.* **2009**, *113*, 893–903. [[CrossRef](#)]
44. USGS, Using the USGS Landsat 8 Product. Available online: [http://landsat.usgs.gov/Landsat8\\_Using\\_Product.php](http://landsat.usgs.gov/Landsat8_Using_Product.php) (accessed on 22 April 2016).
45. Rundquist, D.; Lawson, M.; Queen, L.; Cervený, R. The relationship between the timing of summer-season rainfall events and lake-surface area. *Water Resour. Bull.* **1987**, *23*, 493–508.
46. Xu, H. Modification of normalised difference water index (NDWI) to enhance open water features in remotely sensed imagery. *Int. J. Remote Sens.* **2006**, *27*, 3025–3033. [[CrossRef](#)]
47. Van Zyl, J.J. The Shuttle Radar Topography Mission (SRTM): A breakthrough in remote sensing of topography. *Acta Astronaut.* **2001**, *48*, 559–565. [[CrossRef](#)]
48. Fujita, K.; Suzuki, R.; Nuimura, T.; Sakai, A. Performance of ASTER and SRTM DEMs, and their potential for assessing glacial lakes in the Lunana region, Bhutan Himalaya. *J. Glaciol.* **2008**, *54*, 220–228. [[CrossRef](#)]
49. Collischonn, B.; Collischonn, W.; Tucci, C.E.M. Daily hydrological modeling in the Amazon basin using TRMM rainfall estimates. *J. Hydrol.* **2008**, *360*, 207–216. [[CrossRef](#)]
50. Sorooshian, S.; Hsu, K.L.; Gao, X.; Gupta, H.V.; Imam, B.; Braithwaite, D. Evaluation of PERSIANN system satellite-based estimates of tropical rainfall. *Bull. Am. Meteorol. Soc.* **2000**, *81*, 2035–2046. [[CrossRef](#)]
51. Liu, C.Y.; Liu, G.R.; Lin, T.H.; Liu, C.C.; Ren, H.; Young, C.C. Using surface stations to improve sounding retrievals from hyperspectral infrared instruments. *IEEE Trans. Geosci. Remote Sens.* **2014**, *52*, 6957–6963.
52. Yatagai, A.; Krishnamurti, T.N.; Kumar, V.; Mishra, A.K.; Simon, A. Use of APHRDITE rain gauge-based precipitation and TRMM 3B43 products for improving Asian monsoon seasonal precipitation forecasts by the superensemble method. *J. Clim.* **2014**, *27*, 1062–1069. [[CrossRef](#)]
53. TRMM. Available online: <http://trmm.gsfc.nasa.gov/3b43.html> (accessed on 26 April 2016).
54. Wang, J.; Wolff, D.B. Evaluation of TRMM ground-validation radar-rain errors using rain gauge measurements. *J. Appl. Meteorol. Climatol.* **2010**, *49*, 310–324. [[CrossRef](#)]
55. Zhu, Y.L. Hydro-engineering model on the distribution of factory buildings along the left bank of Jinghong hydroelectric station. *Yunnan Water Power* **2002**, *18*, 98–101. (In Chinese)
56. Cambodia Humanitarian Response Forum (HRF). *Floods Humanitarian Response Forum (HRF) Situation Report No. 06 (as of 08 November 2013)*; Cambodia Humanitarian Response Forum (HRF): Phnom Penh, Cambodia, 2013.
57. Pagano, T.C. Evaluation of Mekong River commission operational flood forecasts, 2000–2012. *Hydrol. Earth Syst. Sci.* **2014**, *18*, 2645–2656. [[CrossRef](#)]
58. Lu, X.X.; Li, S.; Kumm, M.; Padawangi, R.; Wang, J.J. Observed changes in the water flow at Chiang Saen in the lower Mekong: Impacts of Chinese dams? *Quat. Int.* **2014**, *336*, 145–157. [[CrossRef](#)]

